Hybrid PET-optical imaging using targeted probes

Matthias Nahrendorf[1,2], Edmund Keliher[1], Brett Marinelli, Peter Waterman, Paolo Fumene Feruglio, Lioubov Fexon, Misha Pivovarov, Filip K. Swirski, Mikael J. Pittet, Claudio Vinegoni, and Ralph Weissleder[2]

Center for Systems Biology, Massachusetts General Hospital and Harvard Medical School, Boston, MA 02114

Edited by Brian Wilson, University of Toronto, Toronto, Canada, and accepted by the Editorial Board March 16, 2010 (received for review December 31, 2009)

Fusion imaging of radionuclide-based molecular (PET) and structural data [x-ray computed tomography (CT)] has been firmly established. Here we show that optical measurements [fluorescence-mediated tomography (FMT)] show exquisite congruence to radionuclide measurements and that information can be seamlessly integrated and visualized. Using biocompatible nanoparticles as a generic platform (containing a ^{18}F isotope and a far red fluorochrome), we show good correlations between FMT and PET in probe concentration ($r^2 > 0.99$) and spatial signal distribution ($r^2 > 0.85$). Using a mouse model of cancer and different imaging probes to measure tumoral proteases, macrophage content and integrin expression simultaneously, we demonstrate the distinct tumoral locations of probes in multiple channels in vivo. The findings also suggest that FMT can serve as a surrogate modality for the screening and development of radionuclide-based imaging agents.

fluorescence-mediated tomography | molecular imaging | multimodal image fusion | computed tomography

Today, clinical imaging is used largely to provide anatomic, physiological, and metabolic information, but it generally cannot provide information about the underlying molecular aberrations of disease. Molecular imaging probes have the potential to provide such information by interrogating specific targets, such as cell surface receptors, enzymes, and structural proteins. By detecting specific molecular markers, imaging probes could vastly improve the early detection and staging of disease, and thus promote tailoring of targeted therapies for individual patients. There is also considerable interest in identifying and validating surrogate imaging biomarkers as indicators of drug efficacy in clinical trials and medical practice (1).

Increasingly, particular attention has been paid to the development of combined PET–optical molecular imaging agents for translational applications, because these two modalities can provide complementary molecular information. A combined approach would be invaluable for purposes such as whole-body imaging (with, e.g., PET) and subsequent surgical intervention (with, e.g., an intraoperative optical imaging system). Moreover, because preclinical studies can use optical modalities, a combined approach would significantly reduce the hurdles commonly encountered with nuclear imaging and thus accelerate throughput and the development of PET imaging agents. For instance, this strategy would obviate some of the need for expensive equipment, controlled facilities, and a local cyclotron for supplying the radionuclide, and also would reduce the costs associated with handling radioactivity. Furthermore, by targeting the agent toward a surrogate biomarker, its specific localization within the tissue could be visualized via fluorescence; thus, this technique could provide a better understanding of underlying pathophysiology of disease.

A unique platform for the combined development of targeted multifunctional imaging agents is provided by biocompatible nanoparticles (2–5). Such materials have been targeted to endothelial cells (6), growth factor receptors, and specific immune cells (7, 8), and also have been used to report on biological processes, such as phagocytosis (9). The recent introduction of efficient bio-orthogonal chemistries to radiolabel nanomaterials has further accelerated the development of such materials (10, 11). But although considerable progress has been made in the design and synthesis of multifunctional agents (including small molecules), much less is known on how well optical and PET measurements correlate in vivo.

Like PET (12), fluorescence-mediated tomography (FMT) is inherently quantitative, relies on reconstructions of raw datasets, and often uses structural imaging (CT) to visualize molecular information in its correct anatomic reference (13–15). In the present study, we aimed to (*i*) determine the similarities (or differences) between FMT and PET datasets obtained in vitro and in vivo, (*ii*) determine the correlation of signals, (*iii*) ascertain whether FMT agents can be used to design PET imaging agents (or whether there are fundamental differences), and (*iv*) determine whether FMT and PET datasets can be merged into multicolor images in which each color reports on a different biological process, cell type, or pathway in real time. Our findings demonstrate exquisite congruence between optical FMT and PET measurements, and indicate that multichannel FMT/PET-CT fusion can seamlessly integrate and visualize these data. This advance likely will accelerate the development of the next generation of PET/optical molecular imaging agents.

Results

Approach. In this study we used a unique, biocompatible nanoparticle platform for fusion imaging (Fig. 1*A* and Fig. S1). The nanoparticle was based on a well-developed dextranated core-shell nanoparticle [cross-linked iron oxide (CLIO)], similar to a recently FDA-approved nanomaterial. To be suitable for fusion imaging, the dextran surface was first aminated and then reacted with hydroxysuccinimide-derivatized fluorochromes and azides for clicking short ^{18}F-PEGs to the material. When injected i.v., the 30-nm nanoparticles had a blood half-life of ~6 h and were excreted at <5% at 24 h, by which time they had accumulated primarily in macrophages (83%) and to a lesser degree in neutrophils (15%) (Fig. S2). Importantly, the nanoparticles can be further reacted with targeting ligands (peptides, aptamers, antibodies) or other chelators [e.g., for ^{64}Cu (16, 17) or ^{89}Zr labeling (18)]. When labeled with PET isotopes, the specific activities were 37.9 mCi ^{18}F/mg Fe (1.47 GBq/mg Fe) or 34.5 mCi ^{64}Cu/mg Fe (1.28 GBq/mg Fe).

Multimodality image fusion can be achieved with feature recognition (19), contour mapping (20), fiducial matching (13, 15, 21), or other approaches (22). In this study, we adopted the fiducial matching technique, a robust and well-developed method. All images were acquired in a spatially confined imaging cassette with 22 predefined fiducial markers detectable by CT, PET, and optical imaging (Fig. 1*B*).

Author contributions: M.N., E.K., B.M., P.W., M.P., F.S., M.J.P., C.V., and R.W. designed research; M.N., E.K., B.M., P.W., P.F.F., L.F., M.P., F.S., and C.V. performed research; M.N., E.K., B.M., P.W., P.F.F., L.F., M.P., F.S., M.J.P., and C.V. analyzed data; and M.N., E.K., B.M., P.W., M.P., F.S., M.J.P., C.V., and R.W. wrote the paper.

Conflict of interest statement: R.W. is a consultant to VisEn Medical. R.W. and P.W. own VisEn Medical Shares.

This article is a PNAS Direct Submission. B.W. is a guest editor invited by the Editorial Board.

[1]M.N. and E.K. contributed equally to this work.

[2]To whom correspondence may be addressed. E-mail: MNahrendorf@mgh.harvard.edu or rweissleder@mgh.harvard.edu.

This article contains supporting information online at www.pnas.org/cgi/content/full/0915163107/DCSupplemental.

www.pnas.org/cgi/doi/10.1073/pnas.0915163107

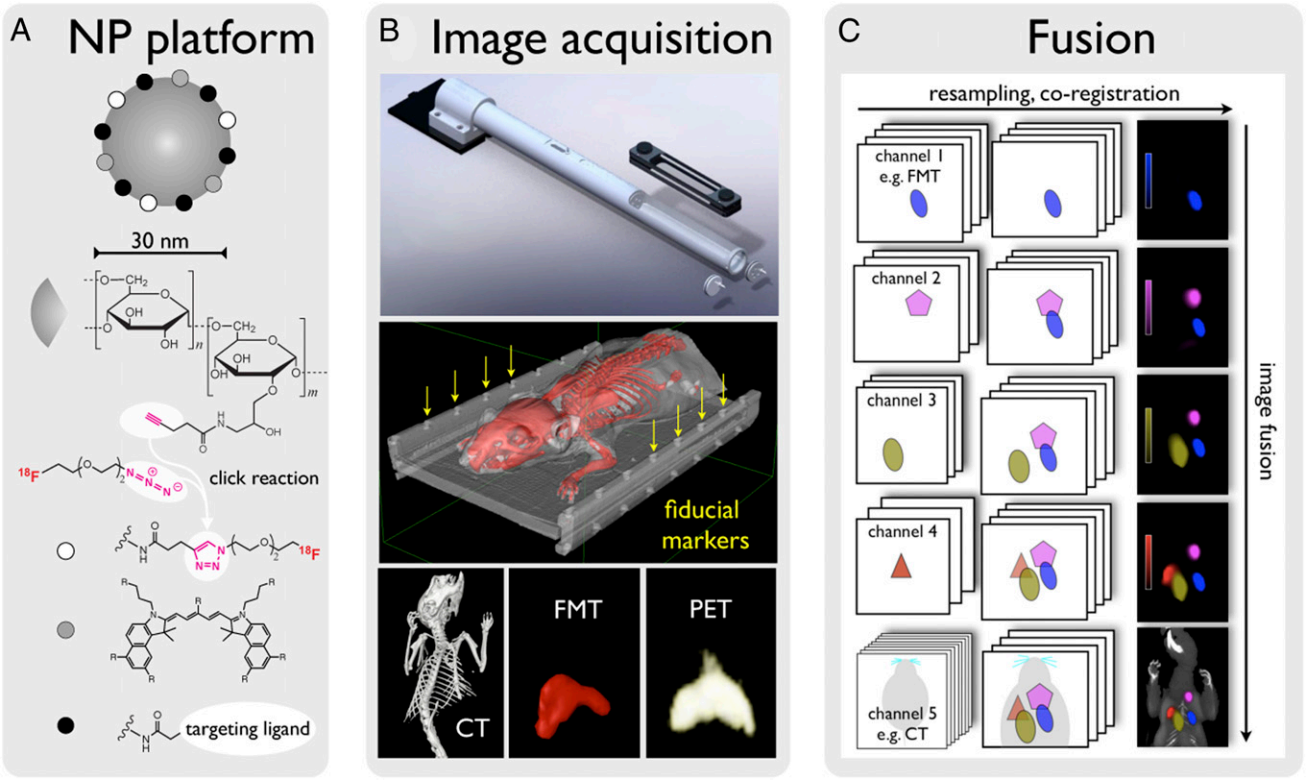

Fig. 1. Approach. (*A*) A 30-nm nanoparticle with an iron oxide core and a dextran shell was used for multimodal imaging. The dextran shell carried ~40 amines per particle, which were used to attach more ligands. The clinical PET isotope ^{18}F was attached with click chemistry. A near-infrared fluorochrome was used for FMT, fluorescence histology, and flow cytometry. These underivatized nanoparticles are avidly taken up by myeloid cells (i.e., monocytes and macrophages). However, this platform also can be derivatized with affinity ligands, such as peptides (6) or small molecules (3). (*B*) (*Top*) An imaging cassette and an adapter specifically developed for use in the Inveon PET-CT platform. This adapter can be fixed to the gurney, allowing seamless positioning of the cassette in the CT and PET ring. (*Middle*) Surface-rendered CT image of a mouse inside the imaging cassette. The lid of the cassette was segmented out to show the fiducial wells that are used for FMT/PET-CT fusion (yellow arrows). (*Bottom*) A 3D reconstruction of a CT, FMT, and PET dataset after injection of ^{18}F-CLIO-VT680 into a control mouse. Nanoparticle signal was predominantly seen in the liver and spleen. (*C*) The algorithm for multichannel fusion based on fiducials. The software plug-in is described in more detail in *SI Methods*. Raw image datasets are resampled and coregistered (horizontal arrow) to match image dimensions, and then fused (vertical arrow). Images on the right were acquired in a four-channel FMT-CT experiment (described in detail in *SI Methods*).

All images were acquired as DICOM data sets and individually exported and stored on a home-built PACS (Picture Archive and Communication System) server. To fuse and visualize images from the three different modalities and channels ($n = 4$ for FMT, $n = 1$ for PET, $n = 1$ for CT), we developed and tested an easy-to-use plug-in for an open-source DICOM viewer (OsiriX). For each fusion, the fiducial markers on the imaging cartridge were selected on individual channels, which then, through drag-and-drop actions, resulted in resampled fused multichannel images, as illustrated in Fig. 1*C*. Fused datasets were stored in the DICOM format. The design and use of the plug-in is described in detail in *SI Methods*.

Signal Linearity and Detection Threshold. Signal linearity and detection thresholds of FMT and PET were initially evaluated in agar-based phantoms, in which wells were filled with serial dilutions of ^{18}F-CLIO-VT680 or ^{64}Cu-CLIO-VT680. Image z-stacks were obtained and rendered in 3D. From these volumes, activities and fluorochrome concentrations were determined based on previous calibration curves. There was excellent correlation between PET and FMT signals, with a correlation coefficient value (r^2) of > 0.99 for ^{18}F-CLIO-VT680 (Fig. 2*A*). Given the specific activities and fluorochrome loading of the nanoparticles in this study, the detection threshold was 0.025 μg Fe/mL by PET and 1.25 μg Fe/mL by FMT. Similar experiments also were conducted with ^{64}Cu-labeled nanoparticles with longer half-lives (Fig. 2*B*). Here the correlation coefficient was >0.99, and the detection threshold was 0.1 μg of Fe/mL by PET imaging. These values are somewhat lower than those achieved with ^{18}F, most likely because of the lower branching ratio of ^{64}Cu (23).

Spatial Coregistration. Because signal congruence is an essential benchmark for any fusion method, we determined the congruence of the fusion approach between FMT and PET. Fusion was based on landmarks on the imaging cassette, and fiducials were aligned using OsiriX. Excellent spatial agreement was obtained after fusion (Fig. 3). The congruence between PET and FMT datasets in the *xy* plane was quantified with a cross-correlation function (CCF) based on Pearson's coefficient (PC), as was applied previously for microscopic imaging (24). The peak correlation coefficient of the 2D signal was 0.85 ($P < 0.05$) when the datasets were at an *xy* translation of 0. When the matrices were intentionally misaligned by inducing predefined relative translations along the *x*-axis and *y*-axis directions, the correlation coefficient decreased rapidly, signifying good coregistration of signal distribution between FMT and PET (Fig. 3).

In Vivo Correlation. Encouraged by the correlation in vitro, we next performed in vivo experiments. We chose to image tumor-associated macrophages in BALB/c mice bearing CT26 colon carcinomas in their flanks. This model system and the nanoparticle distribution has been validated for optical imaging; the nanoparticles preferentially target tumor-associated macrophages (TAMs) (7). All mice underwent PET-CT and FMT 24 h after injection of ^{64}Cu-CLIO-VT680. As expected, both imaging modalities detected a signal in the tumors, and the spatial distribution and amplitude of the signals were well

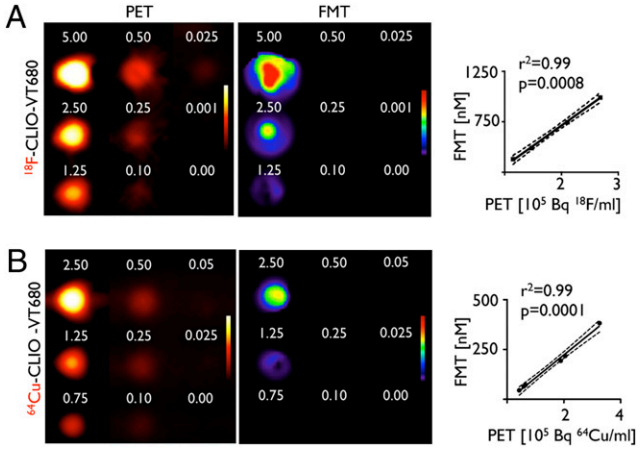

Fig. 2. Signal correlation in phantoms. Two-dimensional images of tissue phantoms, acquired by PET and FMT imaging. ^{18}F-CLIO-VT680 (*A*) and ^{64}Cu-CLIO-VT680 (*B*) were diluted serially, and the concentration was reported according to the iron content in the nanoparticle core. The correlation between FMT and PET signals is shown on the right. FMT signals are reported as fluorescence concentration (nM); PET signals, as counts per volume (Bq/mL).

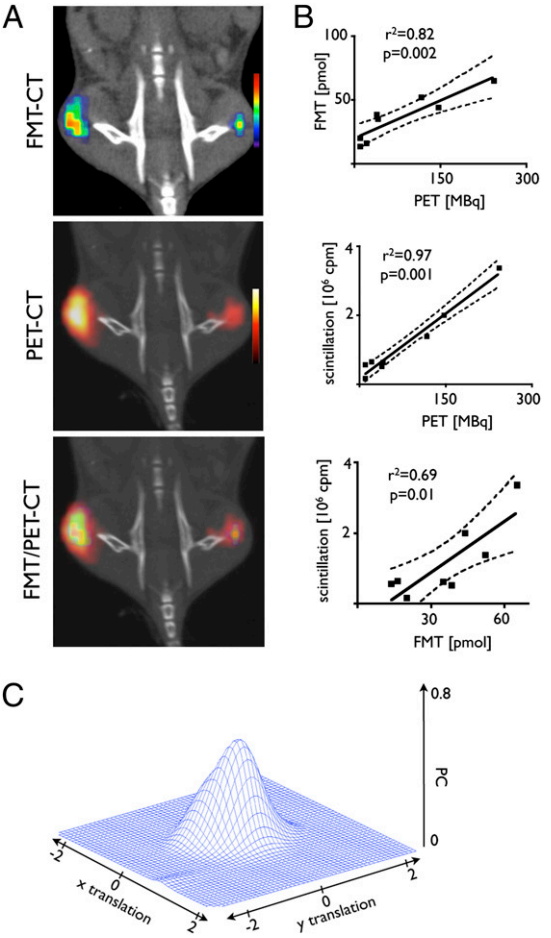

Fig. 4. Comparison of modalities in vivo. (*A*) FMT-CT, PET-CT, and FMT/PET-CT reconstructions of a representative mouse with bilateral flank tumors. The signal intensity was color-coded and was found to correlate well in amplitude and location. (*B*) Correlations of in vivo FMT to in vivo PET signal (*Upper*), ex vivo tumoral activity (measured by scintillation counting) to in vivo PET (*Middle*), and in vivo FMT signal to ex vivo scintillation counting (*Lower*). (*C*) As shown in Fig. 3 for phantoms, signal distribution was compared using the CCF. A good correlation of modalities was found.

correlated (Fig. 4*A*). In coregistered volumes of interest (including individual tumors), the fluorescence concentration measured by FMT correlated well with activity quantified by PET ($r^2 = 0.82$, $P = 0.002$; Fig. 4*B*). After imaging, tumors were excised for ex vivo analysis. In vivo PET and FMT signals for tumors correlated well with the ex vivo gold standard, tissue scintillation (Fig. 4*B*). In parallel to phantom imaging, we also analyzed the colocalization of FMT and PET signals in the *xy* plane using the CCF. In vivo, the correlation was $r^2 = 0.56$ ($P < 0.05$; Fig. 4*C*).

Multichannel Integration. To expand our ability to fuse and simultaneously visualize different molecular markers in vivo, we explored the integration of multichannel optical datasets into the PET-CT framework. Tumor-bearing mice were injected i.v. with three molecular probes: (*i*) the TAM-targeting nanoparticles described above (^{64}Cu-CLIO-VT680), (*ii*) a cathepsin imaging probe (excitation, 750 nm), and (*iii*) an $\alpha_V\beta_3$ integrin imaging probe (excitation, 635nm). The aim of this experiment was to compare the signal distribution of the PET candidate probe with that of independent markers of malignancy, such as high protease activity (25) and integrin expression (26, 27). Spectrally resolved signals were observed in the tumors of all mice (Fig. 5*A*). Quintuple fusion of three FMT channels with PET and CT (Fig. 5*B*) resulted in overall colocalization of signals within the tumor and its immediate vicinity, but with distinct local distributions for a given agent (Fig. 5*C*). To validate these in vivo imaging results, we performed additional in vitro imaging experiments at the macroscopic and microscopic levels (Fig. 6). Overall, in vivo and in vitro fluorescence reflectance and autoradiography data were well correlated (Fig. 6 *A–D*). The integrin signal was highest at the tumor margins, whereas cathepsin activity and phagocytosis were often higher within the tumor bulk. These observations were confirmed microscopically (Fig. 6 *E–J*).

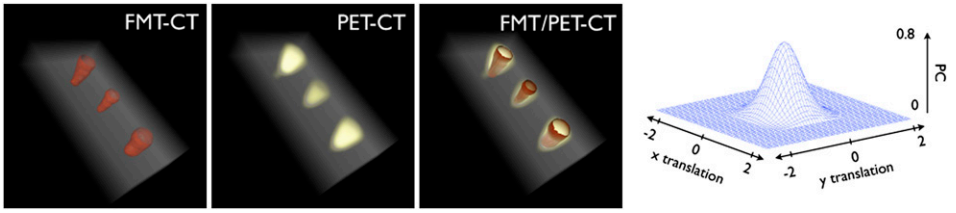

Fig. 3. Coregistration of FMT and PET in tissue phantoms. Three-dimensional, surface-rendered reconstruction of FMT-CT, PET-CT, and FMT/PET-CT images show good correlations in spatial signal distribution. Because of the greater sensitivity of PET, the positive area is slightly larger for this modality. The correlation of spatial FMT and PET signal distributions in coregistered data was quantitated with a CCF (the 3D mesh on the right) based on the PC (perfect coregistration, PC = 1; no coregistration, PC = 0). In high-colocalized conditions, the CCF is close to 1 at its maximum, which occurs for low relative translations, that is, $\Delta x \approx \Delta y \approx 0$. The CCF analysis shown here indicates very good concurrence between the PET and FMT reconstructions.

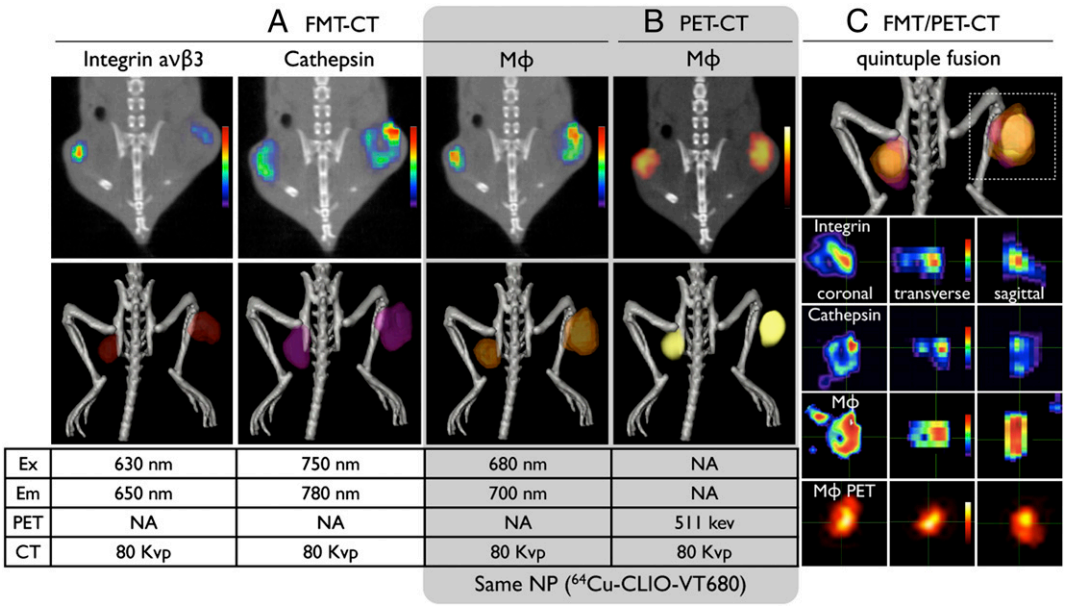

Fig. 5. In vivo multichannel FMT/PET-CT. FMT/PET-CT of tumor-bearing mice, coinjected with a fluorochrome-derived RGD peptide targeting integrin (Integrisense), a protease sensor (Prosense), and the nanoparticle PET agent (^{64}Cu-CLIO-VT680). (*A* and *B*) In 2D images, FMT (*A*) and PET (*B*) signal intensities were color-coded, whereas 3D reconstructions show a surface-rendered signal. (*C*) Overall, the signals in all FMT channels and in PET colocalized in tumors; however, when assessed at higher magnification, distinct differences between probes due to their different target profiles became evident.

Discussion

In vivo imaging is a powerful tool for studying connections between biological processes at different temporal and spatial scales. Recently developed imaging technologies are capable of quantitating a variety of markers in vivo. Of these, the most widely applied is probably fluorescence optical imaging (28), with a number of technologies (e.g., FMT, multiphoton microscopy) already adapted for in vivo experimental use. These techniques are now on the verge of addressing fundamental questions in molecular oncology: How do the molecular and cellular components of signaling pathways interact in vivo? What are the kinetics and flux rates of such networks? What are the differences between pathways in malignant and healthy tissue? Can we identify the dominant regulators that will translate into the most efficient readouts of cancer progression and therapeutic efficacy?

In parallel, various clinical imaging technologies (e.g., PET, CT, MRI) have emerged as sensitive tools for cancer detection, disease staging, and readouts for determining treatment response (29, 30). One of the most significant obstacles hindering the expansion and utility of such methods is the slow development and validation of translatable molecular imaging probes. Although rational design frequently yields first-generation prototypes, agents for clinical use commonly undergo stringent iterative redesign, optimization, and validation procedures, which can take many years. Thus, high-throughput surrogate methods that provide information about the behavior of isotope-labeled agents in vivo would be highly desirable for accelerating agent design and validation. Many of the high-throughput technologies used in today's drug development rely on fluorescence; thus, the development and validation of imaging approaches that bridge the gap between these high-throughput approaches and PET imaging is a worthy goal.

Various requirements must be met before FMT can be used as a surrogate modality for PET agent development, including linearity of signal correlation between modalities, robust coregistration and colocalization of signals, and comparable detection thresholds. Using nanoparticles with fixed fluorochrome/radionuclide ratios and an iron oxide core for signal normalization, we compared preclinical PET and FMT imaging with respect to these criteria. Precise analysis was achieved via a multimodal fusion approach, using an imaging cartridge with fiducial markers in free-space multichannel FMT and a DICOM viewer software module for image fusion. We

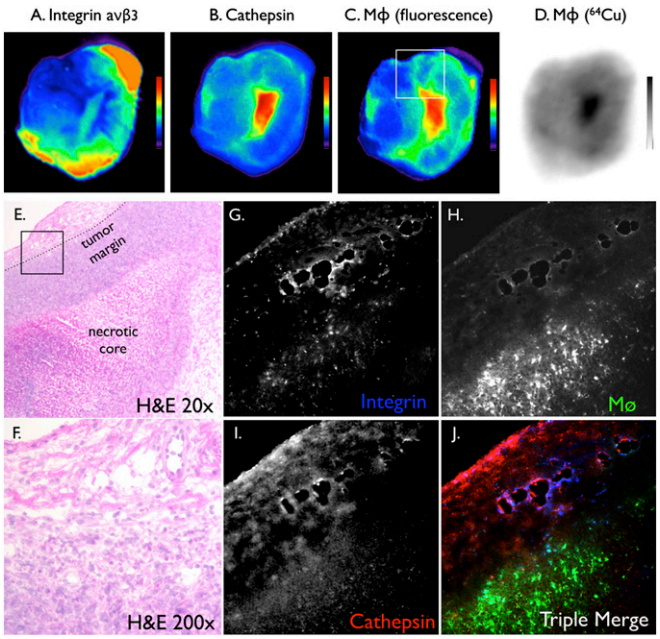

Fig. 6. Ex vivo high-resolution imaging showing differential probe uptake in a tumor. (*A–C*) Ex vivo fluorescence reflectance imaging of the same tumor in respective wavelengths depicting probe distribution of coinjected molecular sensors. The box in *C* shows localization of the histology shown in *E–J*. (*D*) Autoradiography demonstrating a similar signal pattern as that of fluorescence imaging in *C*, because it reports on the same nanoparticle. (*E* and *F*) H&E histology. The box in *E* shows the locations of *F–J*. (*G–J*) Fluorescence microscopy of the same section in respective channels showing differential microscopic distribution of three coinjected probes. The integrin signal is accentuated in the tumor margin in vessel-like structures, whereas the nanoparticles accumulates in TAMs. (Original magnification 200×.)

found excellent correlation of signal amplitudes in phantoms ($r^2 > 0.99$) and in tumor-bearing mice ($r^2 = 0.82$), and noted that both in vivo modalities were well correlated with the ex vivo scintillation of tumor specimens. Importantly, the correlation of signals was linear over a considerable dynamic range. Given the specific activities and fluorochrome loading of the nanoparticles in this study, the detection threshold for PET was ~10-fold better than that for optical imaging. This comparison is somewhat arbitrary, however, because it depends on specific activities and the type of fluorochrome used. Furthermore, detection is time-dependent, because the radiotracer, unlike a fluorochrome, decays.

PET and FMT imaging rely on profoundly different physical principles. In PET, the spatial resolution is limited by the distance that a positron travels after its emission from the parent isotope until its annihilation on encountering an electron. Annihilation of a positron produces two gamma rays, which travel freely through tissue until detected (31). Thus, the origin of the two rays, which signifies an area with high signal in reconstructed PET images, may not precisely colocalize with the isotope location. In contrast, with FMT imaging, the fluorochrome is excited with a laser, which causes it to emit a photon in the exact location of the agent. This emitted photon is subject to absorption while traveling through tissue, however. Scatter is observed in both modalities and is corrected for in respective reconstruction algorithms (*SI Methods*). Given the divergent physics of FMT and PET signal detection, we thought it important to compare the spatial signal distribution of both modalities. The correlation between FMT- and PET-derived signals suggest that even though the aforementioned differences reduce spatial resolution of each modality, FMT/PET fusion imaging is a viable option.

After reconstructing the PET, CT, and FMT datasets using a widely used algorithm (*SI Methods*), we converted data to the DICOM standard and used the fiducial markers on the cartridge identified by CT and FMT for landmark-based coregistration. The data were resampled to match image matrices and dimensions and then fused with the developed plug-in. Each channel was assigned a color look-up table (CLUT), and if signal overlap was detected, colors were mixed accordingly. Especially in situations when multiple FMT channels are fused, the choice of a single-color CLUT, with signal intensity encoded by brightness, might be beneficial (Fig. 1*C*). Each channel can be windowed individually to optimize the dynamic range for viewing. The signal can be quantified either on workstations of respective scanners or, better, in the DICOM viewer, in which regions of interest are drawn on one single-channel image and then copied onto the remaining channels, thereby ensuring identical region size and position. In the system used in this study, we used an imaging cassette to immobilize animals and simplify fusion between modalities via fixed fiducials on the cassette. For certain biological experiments, it is necessary for animals to move between scanning devices. In these scenarios, other fusion techniques would be preferable, such as the use of anatomic landmarks, mutual information, and warping algorithms. This is especially important for temporal examination of animals over multiple-day or -week periods.

The hybrid imaging method reported here has at least three distinct applications: (*i*) It is an experimental tool for parallel visualization of different biological processes in vivo and in real-time, (*ii*) it might accelerate the chemistry of PET agent probe development, and (*iii*) it might advance the clinical management of cancer patients. Fluorescence imaging is increasingly viewed as a valuable intraoperative (32–34) and diagnostic tool (e.g., colonoscopy) (35, 36) for providing molecular information (37). A hybrid PET/fluorescent agent could serve a dual purpose; PET-CT imaging would delineate tumors noninvasively throughout the entire body and facilitate preoperative staging of disease, and also serve as an aid for planning surgery. After 10 half-lives (~18 h for ^{18}F), the isotope on the nanoparticle will have decayed, but the fluorescence tag can still be used for intraoperative optical imaging. For example, probes that demarcate the tumor margin could be used to guide surgical removal of the diseased tissue.

In conclusion, the data presented here demonstrate the sensitivity and quantitative capability of FMT. The predictive nature of biological datasets likely will enable the development of clinical PET reporters. Combined FMT/PET-CT multichannel imaging currently offers parallel interrogation of up to five molecular targets. This capability enhances the simultaneous examination of biomarker clusters, and ultimately improves our understanding of biological systems.

Methods

Nanoparticles. Nanoparticles were prepared as described in *SI Methods*. A click-labeling strategy was used for ^{18}F-labeling of nanoparticles.

Mice. Five C57/BL6 mice were injected with ^{18}F-CLIO-VT680 and used for biodistribution studies 4 h later. The cellular distribution of nanoparticles was assessed by flow cytometry in three additional C57/BL6 mice as described in *SI Methods*. Eight BALB/c mice received s.c. injections with 10^6 autologous colon carcinoma CT26 cells (American Type Culture Collection) into each flank and underwent imaging 10 days later. Five mice underwent single-channel FMT/PET-CT, and three other mice underwent three-channel FMT/PET-CT, followed by ex vivo imaging. Mice were anesthetized (isoflurane 1.5%; O_2 2 L/min) during imaging with a gas delivery system integrated into a multimodal imaging cartridge. The histological analysis is described in *SI Methods*. All animal experiments were approved by Massachusetts General Hospital's Institutional Review Committee.

Image Acquisition. PET-CT images were acquired on a Siemens Inveon unit, and FMT imaging was done with a VisEn Medical FMT-2500 system in three channels (excitation/emission wavelengths 635/655 nm, 680/700 nm, and 750/780 nm). The vendors specify a PET system sensitivity of 10% and a FMT system detection threshold at 1 pmol in a diffusive medium for full tomographic data acquisition with a maximum source density of 1×1 mm. Integrisense-635 and Prosense-750 (VisEn Medical) were injected at doses of 5 and 2 nmol per mouse, respectively. Image acquisition and reconstruction are described in detail in *SI Methods*.

Image Coregistration. PET and CT image reconstructions were converted into the DICOM format, and PET images were coregistered to CT using a preset transformation matrix using native software on the Inveon (IRW; Siemens). Three-dimensional regions of interest were drawn on the fused PET-CT images to encompass individual tumors on the left and right flanks. The average activity value (MBq) for each region of interest was recorded, decay-corrected to a common time point, and correlated to both ex vivo scintillation counts and in vivo fluorescence from FMT. Data were then imported into OsiriX (OsiriX Foundation) to coregister FMT, PET, and CT images. Fiducials on the imaging cartridge were visualized and tagged in FMT and CT images with point markers to define their location in 3D, allowing point-based registration of FMT data to CT coordinates. Using OsiriX's open source, a custom-built plug-in allowed us to simultaneously view and analyze multiple combinations of fused images (*SI Methods*).

Agreement of spatial FMT and PET signal distribution in coregistered datasets was quantitated with a CCF based on PC, which provides a measure of the linear relationship between two different variables, with a value ranging between 0 and 1 (perfect coregistration, PC = 1; no coregistration, PC = 0). Whereas these variables represent signal intensity values in space, we also determined the accuracy of coregistration and visualized the spatial correlation. To do this, we calculated the CCF between the volumetric distribution of the two datasets and translated the volume distribution of one dataset with respect to the other by Δx and Δy along the x and y axes. The CCF thus obtained gives the PC value for each translation. The better the colocalization, the greater the resulting CCF sharpness. In high-colocalized conditions, the CCF is at its maximum (~1), which occurs for exact fusion at low relative translations, that is, $\Delta x \approx \Delta y \approx 0$.

ACKNOWLEDGMENTS. We thank Andita Newton, the Center for Systems Biology Mouse Imaging Program (Yoshiko Iwamoto and Jessica Sullivan), Nikolai Sergeyev, and Wael Yared for technical support and helpful discussions. We also thank Michael J. Welch (Washington University) for providing the ^{64}Cu used in this study. This work was funded in part by National Institutes of Health Grants R01 EB006432, P50-CA86355, R24 CA92782, U54 CA126515, and UO1 HL08073 (to R.W.), R01HL096576 and American Heart Association Grant 0835623D (to M.N.), and the Regione Veneto and CARIVERONA Foundation (P.F.F.).

1. Weissleder R, Pittet MJ (2008) Imaging in the era of molecular oncology. *Nature* 452: 580–589.
2. Choi HS, et al. (2010) Design considerations for tumour-targeted nanoparticles. *Nat Nanotechnol* 5:42–47.
3. Weissleder R, Kelly K, Sun EY, Shtatland T, Josephson L (2005) Cell-specific targeting of nanoparticles by multivalent attachment of small molecules. *Nat Biotechnol* 23: 1418–1423.
4. Welch MJ, Hawker CJ, Wooley KL (2009) The advantages of nanoparticles for PET. *J Nucl Med* 50:1743–1746.
5. LaConte LE, et al. (2007) Coating thickness of magnetic iron oxide nanoparticles affects R_2 relaxivity. *J Magn Reson Imaging* 26:1634–1641.
6. Nahrendorf M, et al. (2006) Noninvasive vascular cell adhesion molecule-1 imaging identifies inflammatory activation of cells in atherosclerosis. *Circulation* 114:1504–1511.
7. Leimgruber A, et al. (2009) Behavior of endogenous tumor-associated macrophages assessed in vivo using a functionalized nanoparticle. *Neoplasia* 11:459–468.
8. Wildgruber M, et al. (2009) Monocyte subset dynamics in human atherosclerosis can be profiled with magnetic nano-sensors. *PLoS One* 4:e5663.
9. Swirski FK, et al. (2009) Identification of splenic reservoir monocytes and their deployment to inflammatory sites. *Science* 325:612–616.
10. Devaraj NK, Keliher EJ, Thurber GM, Nahrendorf M, Weissleder R (2009) ^{18}F-labeled nanoparticles for in vivo PET-CT imaging. *Bioconjug Chem* 20:397–401.
11. O'Reilly RK, Joralemon MJ, Hawker CJ, Wooley KL (2006) Fluorogenic 1,3-dipolar cycloaddition within the hydrophobic core of a shell cross-linked nanoparticle. *Chemistry (Easton)* 12:6776–6786.
12. Di Carli MF, Hachamovitch R (2008) Hybrid PET/CT is greater than the sum of its parts. *J Nucl Cardiol* 15:118–122.
13. Ntziachristos V, Yodh AG, Schnall MD, Chance B (2002) MRI-guided diffuse optical spectroscopy of malignant and benign breast lesions. *Neoplasia* 4:347–354.
14. Guven M, Yazici B, Intes X, Chance B (2005) Diffuse optical tomography with a priori anatomical information. *Phys Med Biol* 50:2837–2858.
15. Nahrendorf M, et al. (2009) Hybrid in vivo FMT-CT imaging of protease activity in atherosclerosis with customized nanosensors. *Arterioscler Thromb Vasc Biol* 29: 1444–1451.
16. Sun G, et al. (2008) Facile, efficient approach to accomplish tunable chemistries and variable biodistributions for shell cross-linked nanoparticles. *Biomacromolecules* 9: 1997–2006.
17. Nahrendorf M, et al. (2008) Nanoparticle PET-CT imaging of macrophages in inflammatory atherosclerosis. *Circulation* 117:379–387.
18. Holland JP, Sheh Y, Lewis JS (2009) Standardized methods for the production of high–specific activity zirconium-89. *Nucl Med Biol* 36:729–739.
19. Behrenbruch CP, et al. (2003) Fusion of contrast-enhanced breast MR and mammographic imaging data. *Med Image Anal* 7:311–340.
20. Mukewar P, Wang G, Henning P, Bao G, Wang M (2004) Segmentation of bionano images for understanding cell dynamics. *Conf Proc IEEE Eng Med Biol Soc* 3: 1759–1762.
21. Deroose CM, et al. (2007) Multimodality imaging of tumor xenografts and metastases in mice with combined small-animal PET, small-animal CT, and bioluminescence imaging. *J Nucl Med* 48:295–303.
22. Meyer CR, et al. (2006) A methodology for registration of a histological slide and in vivo MRI volume based on optimizing mutual information. *Mol Imaging* 5:16–23.
23. Williams HA, Robinson S, Julyan P, Zweit J, Hastings D (2005) A comparison of PET imaging characteristics of various copper radioisotopes. *Eur J Nucl Med Mol Imaging* 32:1473–1480.
24. van Steensel B, et al. (1996) Partial colocalization of glucocorticoid and mineralocorticoid receptors in discrete compartments in nuclei of rat hippocampus neurons. *J Cell Sci* 109: 787–792.
25. Bremer C, Tung CH, Bogdanov AJ, Jr. (2002) Weissleder R (2002) Imaging of differential protease expression in breast cancers for detection of aggressive tumor phenotypes. *Radiology* 222:814–818.
26. Achilefu S, et al. (2005) Synergistic effects of light-emitting probes and peptides for targeting and monitoring integrin expression. *Proc Natl Acad Sci USA* 102:7976–7981.
27. Almutairi A, et al. (2009) Biodegradable dendritic positron-emitting nanoprobes for the noninvasive imaging of angiogenesis. *Proc Natl Acad Sci USA* 106:685–690.
28. Zhou L, El-Deiry WS (2009) Multispectral fluorescence imaging. *J Nucl Med* 50: 1563–1566.
29. Larson SM (2009) Cancer drug development with the help of radiopharmaceuticals: academic experience. *Curr Pharm Des* 15:950–956.
30. Hendee WR, et al. (2007) Biomedical imaging research opportunities workshop IV: A white paper. *Med Phys* 34:673–679.
31. Budinger TF, Benaron DA, Koretsky AP (1999) Imaging transgenic animals. *Annu Rev Biomed Eng* 1:611–648.
32. Kircher MF, Mahmood U, King RS, Weissleder R, Josephson L (2003) A multimodal nanoparticle for preoperative magnetic resonance imaging and intraoperative optical brain tumor delineation. *Cancer Res* 63:8122–8125.
33. Tagaya N, et al. (2008) Intraoperative identification of sentinel lymph nodes by near-infrared fluorescence imaging in patients with breast cancer. *Am J Surg* 195:850–853.
34. Troyan SL, et al. (2009) The FLARE intraoperative near-infrared fluorescence imaging system: A first-in-human clinical trial in breast cancer sentinel lymph node mapping. *Ann Surg Oncol* 16:2943–2952.
35. Kelly K, Alencar H, Funovics M, Mahmood U, Weissleder R (2004) Detection of invasive colon cancer using a novel, targeted, library-derived fluorescent peptide. *Cancer Res* 64:6247–6251.
36. Hsiung PL, et al. (2008) Detection of colonic dysplasia in vivo using a targeted heptapeptide and confocal microendoscopy. *Nat Med* 14:454–458.
37. Veiseh M, et al. (2007) Tumor paint: A chlorotoxin:Cy5.5 bioconjugate for intraoperative visualization of cancer foci. *Cancer Res* 67:6882–6888.